Transmission measurements of hollow-core THz Bragg fibers

Alexandre Dupuis,* Karen Stoeffler, Bora Ung, Charles Dubois, and Maksim Skorobogatiy

École Polytechnique de Montréal, C.P. 6079, Centre-Ville Montreal, Quebec City H3C 3A7, Canada
**Corresponding author: alexandre.dupuis@polymtl.ca*

Received September 29, 2010; revised January 11, 2011; accepted January 11, 2011;
posted January 20, 2011 (Doc. ID 135293); published March 23, 2011

We report on the terahertz (THz) spectral characteristics of hollow-core THz Bragg fibers. Two types of high-index contrast Bragg fibers were fabricated: one based on the index contrast between a polymer and air, and the second based on the contrast between a pure polymer and a polymer composite doped with high-index inclusions. The THz transmission of these waveguides is compared to theoretical simulations of ideal and nonideal structures. Waveguide dispersion is low, and total loss measurements allow us to estimate an upper bound of 0.05 cm^{-1} for the power absorption coefficient of these waveguides in certain frequency bands. We discuss multimode regimes, coupling losses, fabrication difficulties, and how bending losses will ultimately be the discriminant between different THz waveguiding strategies.

OCIS codes: 040.2235, 060.2280, 060.2270.

1. INTRODUCTION

As the applications of terahertz (THz) technology continue to increase [1,2], low propagation loss and low bending loss waveguides are seen as key technology for enabling a more convenient delivery of THz light. Given the finite conductivity of metals and the high absorption loss of dielectrics, it appears that the only viable solution for low-loss propagation is the maximization of the fraction of power propagating in dry low-loss gases. One strategy to achieve this goal is the use of single-mode subwavelength wires with large evanescent fields that extend far beyond the waveguide core into the surrounding gaseous cladding. Both metallic [3] and dielectric [4] subwavelength fibers have been shown to have propagation losses on the order of 0.01 cm^{-1} in the vicinity of 0.3 THz.

A second strategy to increase the fraction of modal power guided in air relies on the use of large hollow-core multimode waveguides. In these waveguides, the propagation loss is proportional to $1/R^3$, where R is the core radius [5–7]. Increasing the core size has lead to record low propagation losses at the expense of entering a multimode regime.

On one hand, metallic guides including metallized tubes and parallel metal plate waveguides have heralded tremendous improvements. First, large hollow-core metallized tubes [8–10] have demonstrated low propagation and bending losses. However, the fabrication technique is based on liquid-phase metal deposition, which limits the fiber length to a few meters. Second, parallel metal plate waveguides [11], traditionally used in a single-mode regime, have recently been shown to support orders of magnitude lower propagation loss in a large-core multimode regime [7,12,13]. The loss of such parallel plate waveguides is now limited by diffraction due to the remaining lack of lateral confinement.

On the other hand, a considerable amount of research has focused on large-core dielectric waveguides, perhaps due to a greater design flexibility for tailoring the waveguiding properties. With the exception of a few solid-core photonic crystal fibers [14–16], research on large-core dielectric THz waveguides has focused on hollow-core dielectric tubes because of the lower absorption loss and lower dispersion that can be achieved by guiding within a gaseous core. Confinement of light within hollow-core dielectric tubes has either been theorized or experimentally demonstrated using a wide variety of cladding reflection schemes: photonic crystal reflection [17–19], attenuated total internal reflection ($n_{clad} < 1$) [20], antiresonant Fabry-Perot reflection [21–23], or Bragg reflection [24,25].

In this paper, we explore the design and fabrication of THz Bragg fibers. Such fibers offer not only the potential for low propagation loss and low bending loss, but a suitable fiber design can also induce an effectively single-mode waveguiding regime [26]. Although there has been a large amount of research on planar THz Bragg reflectors [27–32] and a few theoretical studies proposing THz Bragg fibers [24,25], to our knowledge we present the first experimental realization of such fibers in the THz regime. Moreover, although near-infrared Bragg fibers have demonstrated low propagation losses [6,33,34], a high-index contrast between the high- and low-index layers of the cladding multilayer reflector is required. This high-index contrast is difficult to achieve in the THz regime due to the similarity in the refractive indices of dielectrics such as polymers [35]. Special measures must be taken to increase the refractive index contrast between the layers of a Bragg reflector. We therefore report on two different implementations for increasing the index contrast. The first method is based on the index contrast between a polymer and air, whereas the second is based on the index contrast between a pure polymer and polymer composite doped with high-index inclusions (such as TiO_2 particles within a polyethylene host). THz transmission measurements were subsequently made with a versatile THz-TDS (time domain spectroscopy) setup, which has an adjustable optical path length specially designed for the transmission measurements of waveguides up to 50 cm in length [36].

The paper is organized as follows. Section 2 summarizes the waveguiding principle. Section 3 details the novel fabrication methods. Section 4 presents the experimental transmission and loss measurements. Section 5 models the waveguide losses and attempts a theoretical fit of the experimental transmission spectra. Section 6 explores the fundamental theoretical differences between the two types of Bragg fibers under study and proposes more efficient Bragg fiber designs. Finally, Section 7 concludes with general remarks concerning propagation losses, coupling issues, bending losses, fabrication difficulties, and the possibility of an effectively single-mode regime.

2. WAVEGUIDING PRINCIPLE

A Bragg fiber consists of a circularly symmetric Bragg reflector [see Fig. 1(a)] that confines light to the fiber core. Although Bragg fibers at visible and near-infrared wavelengths can have solid cores, Bragg fibers at THz frequencies require large hollow cores to avoid material absorption loss. The Bragg reflector itself consists of a periodic stack of alternating high- and low-refractive index layers, within which multiple reflections create constructive interference bands of high reflectivity (band gaps of cladding transmission). These reflectivity bands can be tuned arbitrarily by a suitable choice of refractive indices and thicknesses for the Bragg layers. Moreover, larger reflections (and hence lower propagation loss) as well as wider Bragg mirror reflection peaks (fiber transmission windows) will result from a larger index contrast between the constituent layers of the Bragg mirror. Readers should refer to the literature for more information about Bragg fiber theory [6,37,38]; however, a main point that should be emphasized is that propagation losses scale according to $f^{-2} \cdot d_{\text{core}}^{-3}$, where d_{core} is the diameter of the core and f is the frequency of the confined light.

3. FABRICATION METHODS

A. Air-Polymer Bragg Fibers

There exist two fabrication techniques that exploit air in order to increase the refractive index contrast between the layers of a Bragg reflector. The first is a physical separation of the material layers via the use of spacers or bridges that maintain a distance between the material layers, thus creating an air gap (air layers)[28]. The second method consists of fabricating highly porous material layers, whereby porosity effectively reduces the refractive index of a layer [30] until it is close to that of air. In both cases, the size of the features (spacers or porous air bubbles) in the low-index layers must be small enough to reduce the effects of scattering. Although certain polymers can be made to foam by including gas-forming additives within the polymer, processing such porous polymers into fibers is difficult. Instead, we implemented the first method by rolling a polymer film with powder particles. The process is schematized in the first column of Fig. 1. A polydisperse poly (methyl methacrylate) powder, with an average particle size of 150 μm, was randomly laid out on top of two touching 127 μm polytetrafluoroethylene (PTFE) films. The films were subsequently rolled around a mandrel to form the Bragg fiber. The powder particles acted as spacers to maintain an air gap between the spiraled polymer film layers. The film was held together by wrapping it in PTFE tape and the mandrel was removed. The spiral cross section of the fiber, shown in Fig. 1(c), approximates the ideal circularly symmetric structure shown in Fig. 1(a). The final air-polymer Bragg fiber had an inner diameter of 6.73 mm and a reflector of five bilayers consisting of 254 μm PTFE and roughly 150 μm air layers.

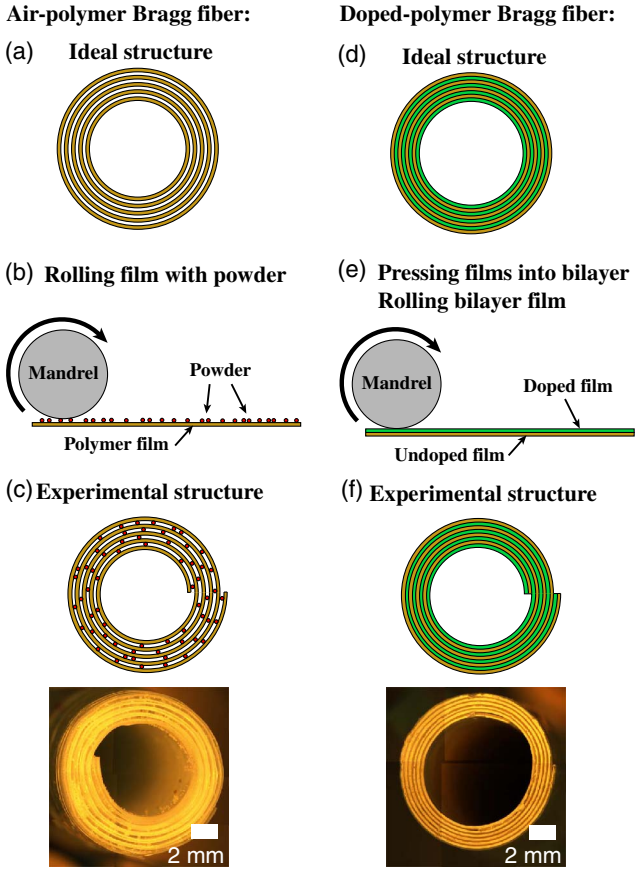

Fig. 1. (Color online) Schematization of the fabrication process of THz Bragg fibers. First column, air-polymer Bragg fiber. Second column, doped-polymer Bragg fiber. The ideal geometry is circularly symmetric; however, the rolling of films creates a spiral defect that breaks the symmetry. Cross-section pictures of the experimental fibers are also shown.

B. Doped-Polymer Bragg Fibers

The second method that we implemented was inspired by the work of Jansen *et al.* [31,39]. They demonstrated that doping a host polymer [like polypropylene (PP)] with high refractive index TiO_2 particles could significantly increase its THz refractive index. We similarly added TiO_2 particles to polyethylene (PE). For the TiO_2 particles, we used R104 grade powder purchased from Dupont, with an average particle size of 0.22 μm. The host polymer was linear low-density polyethylene, grade Sclair FP120A (Nova Chemicals). A mixture of 80 wt.% (46 vol.%) TiO_2 powder in PE was prepared using a twin-screw extruder. The extrudate was cut into pellets and subsequently extruded into film using another extruder. Figure 2 presents the refractive index (n) and power absorption coefficient (α) obtained from THz-TDS measurements of the doped and undoped PE films. Despite some Fabry-Perot oscillations due to the thickness of the samples, the results clearly indicate a substantial increase of the refractive index at high doping concentrations; we find $n = 3$ for 80 wt.% (46 vol.%) R104 grade doping. Moreover, the loss is seen to increase substantially with frequency and can be modeled

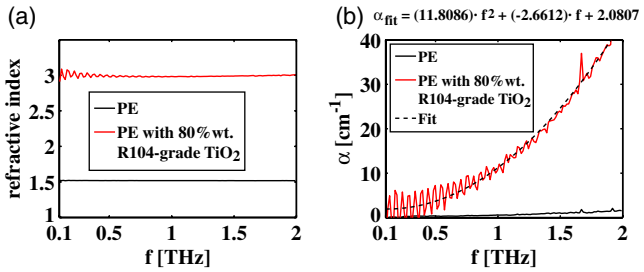

Fig. 2. (Color online) THz refractive index (a) and power absorption loss (b) of pure and TiO_2-doped polyethylene films. Fabry–Perot oscillations due to the thickness of the samples can be seen. Absorption loss from the doped film can be approximated by a quadratic function.

empirically with a quadratic function. In comparison, Jansen *et al.* reported $<5\,cm^{-1}$ absorption loss for 60 vol.% rutile TiO_2 in PP [32], but for frequencies $f < 0.5$ THz.

It should be noted that the high concentrations of powder change not only the refractive index but also the thermomechanical properties of the polymer. The composite material had a higher viscosity and a much higher melting temperature than pure PE. As a result, the extrusion into film was much more difficult and only thick films ($\sim 400\,\mu m$) were obtained. Moreover, the doped-polymer film was brittle. The extruded film was consequently too thick to form a Bragg reflector that would efficiently reflect at frequencies in the 1 THz range. The film, therefore, needed to be pressed to a smaller thickness. Without a roller press to continuously press film down to the proper thickness we had to repeatedly press small film strips using a simple hydraulic press.

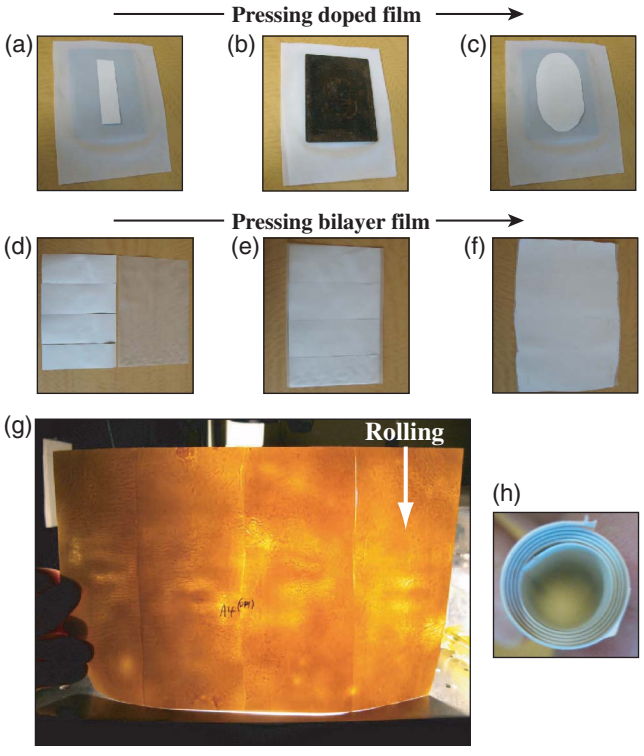

Fig. 3. (Color online) Fabrication steps of a TiO_2-doped polymer Bragg fiber. (a)–(c) Strips of TiO_2 film ($\sim 400\,\mu m$ thick) are pressed to a thinner thickness ($\sim 100\,\mu m$). (d)–(f) High- and low-index films are pressed together to form a bilayer. (g) defects in the bilayer. (h) Bilayer is rolled into a Bragg fiber.

In order to increase the quality of the dielectric interface between the high- and low-index layers of the Bragg reflector, a bilayer film was formed by pressing doped and undoped films together with a hot press. The bilayer fabrication steps are illustrated in Fig. 3. An ~ 400-μm-thick doped-PE film (80 wt.% TiO_2) was cut into strips (see Fig. 3(a)), placed between two PTFE sheets and two metal plates (Fig. 3(b)), and squished to a $\sim 100\,\mu m$ thickness (Fig. 3(c)) using a hot press. The thinner doped film was again cut into strips (Fig. 3(d)) and a sheet of pure PE film was placed on top of the strips (Fig. 3(e)). The low-index undoped PE film was 101.6-μm-thick commercial low-density polyethylene film (McMaster-CARR). The stack of doped/undoped polymer films was hot-pressed together (Fig. 3(f)) to consolidate the bilayer. Note that the pure PE film acts as a glue to stick the doped film strips together and also reduces the brittleness of the film. Although a bilayer film was successfully made, this fabrication process is far from ideal. Figure 3(g) presents many bilayer film defects including density inhomogeneities, cracks in the film, and edge defects between the film strips.

A Bragg fiber was nevertheless fabricated from the resulting bilayer. The bilayer was rolled into a Bragg fiber (see Figs. 1(d) and 3(h)) and solidified in an oven at 130 °C. The spiral cross section of the final fiber, shown in Fig. 1(f), approximates the ideal circularly symmetric structure shown in Fig. 1(d). The final doped-polymer Bragg fiber had an inner diameter of 6.63 mm and a reflector of six bilayers consisting of 135 μm high-index layers of 80 wt.% TiO_2 doped PE and 100 μm low-index layers of undoped PE.

4. TRANSMISSION AND LOSS MEASUREMENTS

The Bragg fiber transmission spectra were measured using the THz-TDS setup schematized in Fig. 4(a). This versatile setup, based on the adjustment of the optical path length by the translation of a mirror assembly, has been described in detail elsewhere [36]. The samples were held in place with the aid of irises and the endpoints were positioned in the focal planes of parabolic mirrors. All samples were measured in a dry nitrogen environment although some residual water vapor was present.

The beam profile of the input beam was assumed to be Gaussian, and the beam size at the input focal plane was measured using a knife-edge technique. Figure 4(b) presents the frequency-dependent FWHM of the Gaussian input beam, calculated from the power spectra of time scans measured at different knife-edge positions. Note that this knife-edge measurement was done at ambient humidity and that certain variations in beam size are attributable to power fluctuations in the vicinity of water vapor absorption peaks (highlighted with red vertical lines).

Figures 4(c) and 4(d) present the time scans of the guided THz pulses. The dispersion is seen to be very low because of the minimal pulse spreading and the high fraction of power guiding within the air. The transmission spectrum of an air-polymer Bragg fiber, 21.4 cm in length, is shown in Fig. 4(e), whereas the transmission spectrum of a doped-polymer Bragg fiber, 22.5 cm in length, is shown in Fig. 4(f). Note that both Bragg fibers display wide transmission peaks; however, the transmission is lower in the case of the doped Bragg fiber. As will be demonstrated in the next section, the waveguides

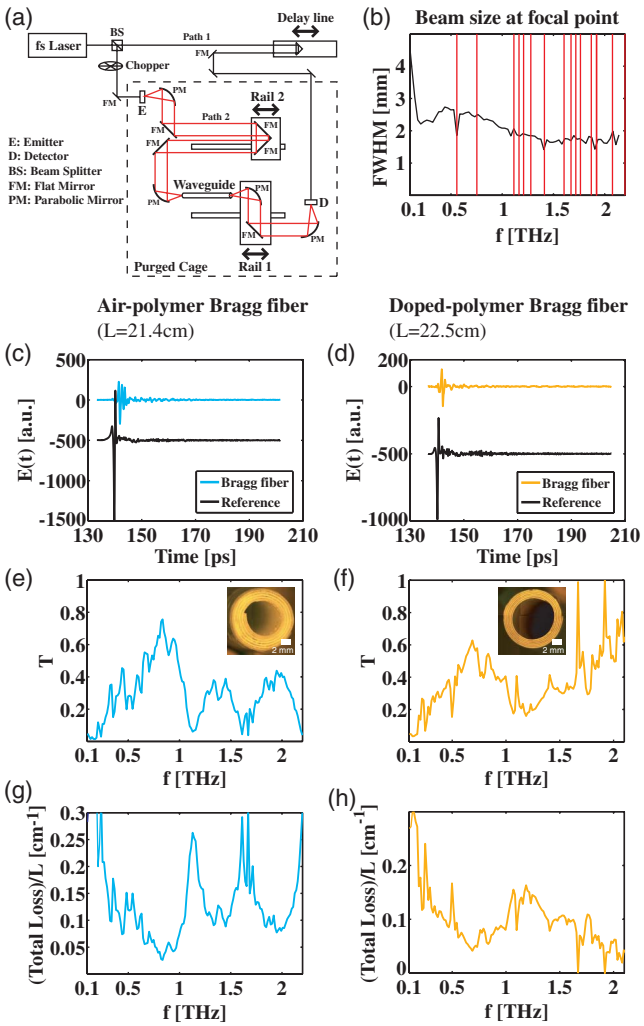

Fig. 4. (Color online) Comparison of the THz-TDS transmission characteristics of air-polymer and doped-polymer Bragg fibers. Left column, air-polymer Bragg fiber. Right column, doped-polymer Bragg fiber. (a) Schematization of THz-TDS setup, (b) FWHM of input beam, (c), (d) time-domain scans, (e), (f) normalized amplitude transmission spectra, (g), (h) uipper bound on propagation loss given by total loss normalized with respect to waveguide length.

are multimode and the shape of the amplitude transmission curves depend on the modal interference between the excited modes. Cutback measurements were attempted in order to measure the propagation losses; however, sample deformation during cutting and slight waveguide misalignment led to significant coupling variations. The resulting changes in modal interference led to complex and variable spectra making the cutback technique impracticable. We nevertheless estimate an *upper bound* on the power propagation loss coefficient α by plotting, in Figs. 4(e) and 4(f), the total transmission loss normalized with respect to the waveguide length $(-2\ln(|T|)/L)$. The lowest total loss points yield $\alpha < 0.028\,\mathrm{cm}^{-1}$ at 0.82 THz for the air-polymer Bragg fiber, and $\alpha < 0.042\,\mathrm{cm}^{-1}$ at 0.69 THz for the doped-polymer Bragg fiber.

5. THEORETICAL MODELING OF TRANSMISSION

In order to better understand the results of Fig. 4, exact vectorial simulations were carried out to calculate the modal propagation losses and coupling efficiencies. The simulations use the experimental dimensions of the Bragg fibers that were given in Section 3. It should be noted that the experimental Bragg fibers and the Bragg fiber simulations throughout this paper consider a core/cladding interface with a high-index layer as the first layer of the periodic multilayer cladding. Although the bandgap frequencies would remain unchanged if a low-index layer was used for the first layer, it is advantageous to use a high-index layer as the first layer because the higher reflectivity at the core-cladding interface reduces the modal loss [37]. Furthermore, the simulations assumed material parameters taken from the literature [35]: $n_{\mathrm{PTFE}} = 1.44$ and $\alpha_{\mathrm{PTFE}} \sim 1\,\mathrm{cm}^{-1}$ for the high-index layers of the air-polymer Bragg fiber, as well as $n_{\mathrm{PE}} = 1.534$ and $\alpha_{\mathrm{PE}} \sim 1\,\mathrm{cm}^{-1}$ for the low-index layers of the doped-polymer Bragg fiber. For simplicity, frequency independent values were assumed for the pure polymer material parameters. Section 3.B presented the THz material parameters of the TiO_2-doped PE. In Fig. 2, it can be seen that a constant index of $n_{\mathrm{DopedPE}} = 3.0$ can be assumed and that the absorption coefficient of the doped polymer can be empirically fitted with a parabola: $\alpha_{\mathrm{DopedPE}} = (11.8086)\cdot f^2 - (2.6612)\cdot f + (2.0807)$, where α is in cm^{-1} and f is in THz. This formula was used in the simulations for the power loss in the high–refractive–index layers of the doped-polymer Bragg fiber.

Because of the rolling of polymer films in the fabrication process, the Bragg fibers have a spiral edge defect. We began by verifying how the nonideal spiral geometry affected the waveguide transmission. On one hand, a transfer matrix mode solver was used to calculate the exact solutions to Maxwell's equations for a *circular* geometry with an arbitrary number of layers [40]. The field solutions in a circular geometry are a linear combination of Bessel functions. Transfer matrices containing complex-valued Bessel functions are used to construct an eigenvalue problem to satisfy the continuity conditions of the fields in the radial direction [40]. The solutions to the eignevalue problem give the modal parameters (effective propagation index and loss) of the HE and TE modes that are solved for. On the other hand, the finite element mode solver COMSOL Multiphysics is used to calculate the modes of the *asymmetric* spiral geometry.

In the first row of Fig. 5, the propagation losses of the HE_{11} mode of ideal circular waveguides (solid red line) are compared to the losses of nonideal spiral waveguides (circles and crosses). There is good agreement between the results, for both the air-polymer Bragg fiber Fig. 5(a) and the doped-polymer Bragg fiber Fig. 5(b), indicating that the spiral defect does not significantly effect the mode propagation losses. This is reasonable because the edge defect is much smaller than the core diameter. The breaking of the circular symmetry does, however, create a form birefringence. As a result, the polarization degeneracy is lifted and there is a very slight difference between the x- and y-polarized modes. Nevertheless, the birefringence between the x- and y-polarized modes is small with $\Delta n = |n_x - n_y| \le 2\times 10^{-5}$ for the air-polymer Bragg fiber and $\Delta n = |n_x - n_y| \le 8\times 10^{-5}$ for the doped-polymer Bragg fiber. Furthermore, the second row of Fig. 5 compares the power distribution and the orientation of the electric field vectors of the HE_{11} modes of doped-polymer Bragg fibers using either the circular Fig. 5(c) or spiral geometries Fig. 5(d). It can be seen that the modes

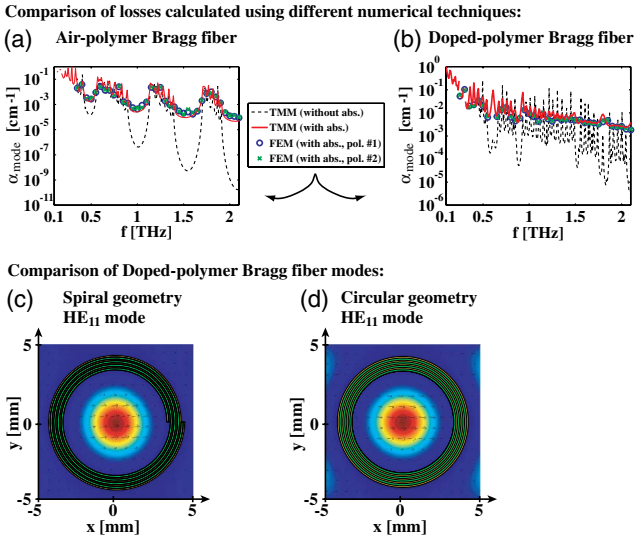

Fig. 5. (Color online) Comparison of the theoretical HE_{11} mode propagation losses of a doped-polymer Bragg fiber with ideal (circular) and nonideal (spiral) geometry. The propagation losses in the case of the circular geometry are calculated using a transfer matrix method (TMM). The solid and dashed lines, respectively, correspond to simulations with and without material absorption. The propagation losses in the spiral geometry (circles and crosses) were calculated with a finite element method (FEM) mode solver. The dimensions and material parameters are described in the text. (a) Air-polymer Bragg fiber, (b) doped-polymer Bragg fiber. There is good agreement between the results indicating that the spiral defect does not significantly effect fiber losses. The similarities are further illustrated by comparing the power distribution and electric field orientation of the HE_{11} mode in the spiral (c) and circular (d) geometries. The modes are seen to be nearly identical.

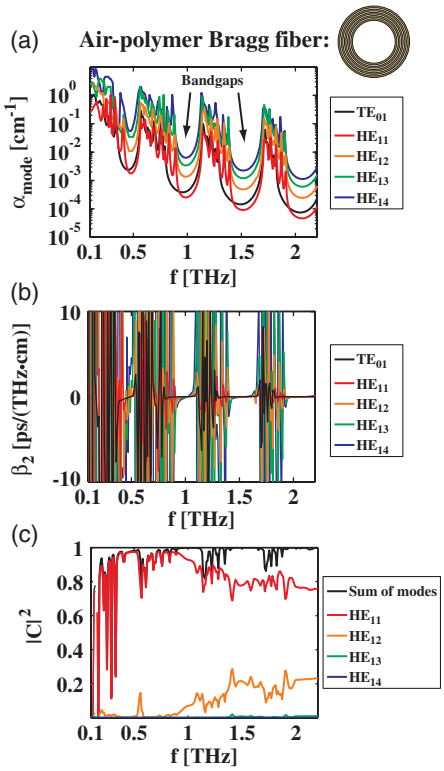

Fig. 6. (Color online) Theoretical modeling of the first few HE modes of an air-polymer Bragg fiber. (a) Power propagation loss coefficient α for the four first HE modes, compared to that of the TE_{01} mode. Note that α includes the effects of absorption and radiation losses. (b) β_2 dispersion parameter. (c) Power coupling coefficients $|C|^2$ for the first four HE modes. Dimensions of the simulated geometry are given in the text.

of the circular and spiral geometries are nearly identical, further indicating that the differences are minor when the core diameter is larger than the wavelength of guided light. Because of the similitude of these results, all subsequent calculations were made assuming an idealized circular geometry.

It should also be noted that the first row of Fig. 5 presents a comparison between the propagation losses calculated with (solid line) and without (dashed line) material absorption. The calculated power propagation losses include both radiation and absorption loss contributions. The radiation loss in the absence of material absorption indicates that, because of a high–refractive–index contrast between the layers of the Bragg reflector, an efficient reflection (low radiation loss) can be achieved even with as few as five bilayers in the reflector. However, the limiting factor is the absorption loss. Ideally, a THz waveguide would be longer than 1 m, requiring a propagation loss smaller than $0.01\ \mathrm{cm}^{-1}$. Whereas the air layers greatly help to reduce the absorption loss in the air-polymer Bragg fiber (Fig. 5(a)), the significant absorption in the doped polymer is seen to limit the propagation loss of the doped-polymer Bragg fiber (Fig. 5(b)).

Figures 6 and 7 respectively present the power propagation losses and dispersion curves of the first few modes of the air-polymer Bragg fiber and the doped-polymer Bragg fiber, calculated using the transfer matrix method and including material absorption. In addition to the first four HE (hybrid electric) modes, the TE_{01} mode (in black) is presented to more clearly illustrate the expected positions of the bandgaps. The Bragg reflector bandgaps define transmission windows of low loss. From Fig. 6(b) it can also be seen that modal dispersion ($\beta_2 = (1/2\pi c)(f \cdot \partial^2 n_{\mathrm{eff}}/\partial f^2 + 2 \cdot \partial n_{\mathrm{eff}}/\partial f)$) is negligible within the bandgaps. This is especially true of the TE_{01} mode. Both of these effects result from the power being confined mainly within the air core when the Bragg reflection is efficient.

The analysis of the doped-polymer Bragg fiber (Fig. 7) is slightly more complicated. Whereas the TE_{01} mode clearly presents bandgaps, the HE modes do not. The difference in loss arises from a difference of field penetration into the cladding, as the fields of the HE modes penetrate farther into the cladding than the TE_{01} mode [40]. In Fig. 2 the absorption loss of the doped polymer is seen to increase rapidly with frequency. Consequently, as the frequency increases, the HE mode penetration within the Bragg reflector becomes limited by absorption and the resonant oscillations due to Bragg reflections are seen to attenuate and disappear.

Note another qualitatively different behavior between the two types of Bragg fiber. On one hand, the doped-polymer Bragg fiber has the TE_{01} mode as the lowest-loss mode. On the other hand, the air-polymer Bragg fiber has the HE_{11} mode as the lowest-loss mode. It is novel that the HE_{11} mode becomes the lowest-loss mode without forcing a single-mode regime with a small core size. The origin of this difference will be discussed in detail in the next section.

We now seek to model the transmission spectra of the multimode Bragg fibers. The total multimode amplitude transmission of the waveguide can be modeled by the following equations [13]:

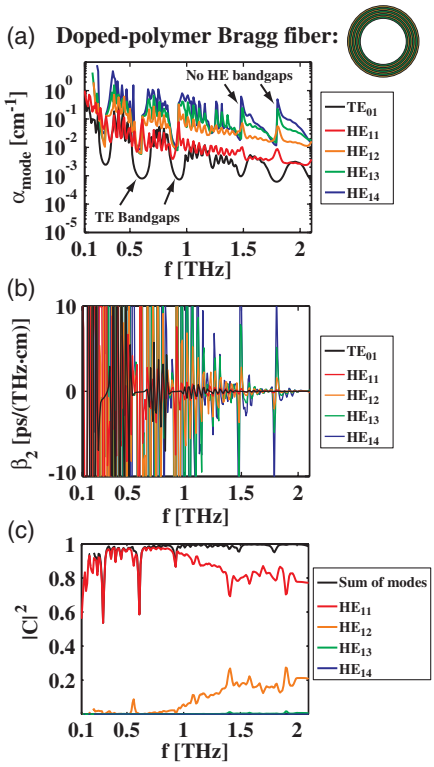

Fig. 7. (Color online) Theoretical modeling of the first few HE modes of a doped-polymer Bragg fiber. (a) Power propagation loss coefficient α for the four first HE modes, compared to that of the TE_{01} mode. Note that α includes the effects of absorption and radiation losses. (b) β_2 dispersion parameter. (c) Power coupling coefficients $|C|^2$ for the first four HE modes. Dimensions of the simulated geometry are given in the text.

$$E_w(f) = |E_r(f)| \cdot \sum_m C_m^{in} \cdot C_m^{out} \cdot e^{i(n_{eff,m}-1)\frac{2\pi f}{c}L} e^{-\frac{\alpha_m L}{2}}, \quad (1)$$

$$|T| = \frac{|E_w(f)|}{|E_r(f)|} = \left| \sum_m |C_m|^2 \cdot e^{i(n_{eff,m}-1)\frac{2\pi f}{c}L} e^{-\frac{\alpha_m L}{2}} \right|, \quad (2)$$

where $E_w(f)$ is the modal field coming out of a waveguide of length L, and $E_r(f)$ is the reference signal measured in the absence of the waveguide at the position of the coupling plane. c is the speed of light, and f is the frequency. The sum is taken over the number of considered modes and the subscript m refers to a given mode. C_m^{in} and C_m^{out} are, respectively, the input and output amplitude coupling coefficients with respect to the waveguide. Since the input and output coupling conditions are assumed to be the same, we have $C_m^{in} \cdot C_m^{out} \approx |C_m|^2$, equivalent to a power coupling coefficient. α_m and $n_{eff,m}$ are, respectively, the power propagation loss coefficient and effective propagation index of the mode guided by the waveguide. Note that the sum of complex exponentials translates into sinusoidal modal interference terms.

The use of Eq. (2) requires the knowledge of the coupling coefficients. To evaluate the coupling coefficients we calculated the overlap integrals between the fields of a guided mode and the field of the input beam. The beam profile of the input beam was assumed to be Gaussian, and the field is approximately a plane wave in the focal plane of the parabolic mirror. The frequency-dependent size of the Gaussian input beam is taken from Fig. 4(b). Since the linearly polarized source favors coupling to the HE modes, Figs. 6(c) and 7(c) present the calculated power coupling coefficients $|C|^2$ for the first four Bragg fiber HE modes. Because of a mismatch between the profiles of the higher-order modes and the input beam, the power coupled to higher-order modes decreases rapidly. In fact, from the sum of the modal powers it can be seen that the first four HE modes account for ~95% of the input power at most frequencies. Therefore, the first four modes were considered to be sufficient for a calculation of the theoretical Bragg fiber transmission spectrum. Moreover, despite the *overmoded* regime of the waveguide, a single mode can be predominantly excited by the proper optimization of the coupling. It can be seen that a majority of the power is coupled to the HE_{11} mode because its bell-shaped profile is a better match to the Gaussian input, especially at low frequencies where the input beam size is larger. However, at high frequencies a significant amount of power (~20%) is coupled into the higher order modes, and interferometric beating between the modes will become pronounced.

Using the propagation losses and coupling coefficients of Figs. 6 and 7, we now compare the experimental transmission curves to a theoretical fit using Eq. (2). Figures 8(a) and 8(b) compare the results of the air-polymer and doped-polymer Bragg fibers respectively. In both cases the model is seen to give a relatively poor fit. Although the theoretical curves describe the general behavior properly there are noticeable differences with respect to the experimental curves. This is due in part to the limited number of modes considered but is mainly attributed to the many fiber defects which are not considered in the simulations.

For instance, in Fig. 8(a) there is a reasonable correspondence between the major Bragg peaks at low frequency, but at high frequency the peaks appear shifted. Such spectral deformations can be attributed to the imperfections seen in the fiber cross section. The co-rolling of two PTFE films without additional solidification has lead to interfacial defect regions with extra air gaps between the films of high index. These air gaps create reflections at extra interfaces and modify the thickness of the high-index layers. Furthermore, the overall transmission is lower than the theoretical prediction in part

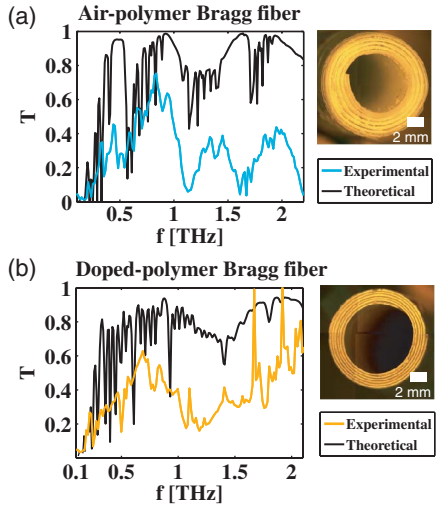

Fig. 8. (Color online) Theoretical fit of the transmission through air-polymer and doped-polymer Bragg fibers. Parameters for the fits are taken from Figs. 6 and 7. Complex oscillations within the spectra are explained by multimode interference [Eq. (2)].

because scattering losses, notably from the powder particles in the low-index layers, have been neglected. Nevertheless, clear bandgaps are visible in the transmission spectrum due to the lowered HE_{11} loss.

In the case of the doped-polymer Bragg fiber, there are thickness variations in the layers of the Bragg reflection due to the pressing of the films. We also suspect inhomogeneities in the dopant density because of the difficulty in uniformly mixing the TiO_2 powder at such high concentrations. Variations in density would result in variations of the refractive index of the Bragg layers. Consider also the many defects in the current doped-polymer bilayer film (Fig. 3(g)). In Fig. 8(b) there are no appreciable bandgaps, and the differences with respect to theory are attributed to neglected scattering effects.

Such fiber defects can be mitigated by better fabrication techniques. One method to increase the quality of the experimental Bragg fibers is to use less absorbing doping materials at lower concentrations in order to conserve the mechanical properties of the polymer host. One such solution is proposed in the next section. Another method is to reduce interfacial defects between the reflector layers by rolling a multilayer film instead of rolling two single-layer films. Multilayer polymer films can be made by co-extrusion of different polymers. Recently, a four-layer film of alternating polystyrene and polymethyl methacrylate layers was co-extruded and processed into a Bragg fiber with lower loss than fibers made by co-rolling individual films [41]. Furthermore, it should be noted that the length of the fibers and the number of bilayers within the reflector is currently limited by the size of the film that was available for rolling. Extrusion would yield larger film that could be rolled into longer Bragg fibers with a greater number of bilayers.

6. BRAGG FIBER DESIGN CONSIDERATIONS

Despite the current fabrication difficulties, Bragg fibers have a tremendous potential for guiding THz radiation with low propagation and low bending losses. In the previous section we saw that the two types of Bragg fibers that were fabricated have fundamentally different operating regimes. To fully appreciate the differences between these two regimes of operation and to design better Bragg fibers, we shall now compare the rate at which the fields of the TE and TM polarizations decay within the Bragg reflectors and see how the TE, TM, and HE mode losses are affected.

The analysis presented in this section closely follows the presentation of [37]. However, in addition to the standard textbook presentation of band diagrams to find the bandgaps of a Bragg reflector [38], here we put emphasis on the calculation of the field decay rates within the Bragg reflector. Novel field decay rate diagrams offer insight into the propagation and bending losses of TE and TM modes. They will also be shown to aid in the design of Bragg fibers.

To examine the field decay, we consider the propagation through semi-infinite multilayer Bragg reflectors, where a transfer matrix can be constructed to relate the fields in one layer to the fields of a subsequent layer. The following analysis relies on the Bloch theorem [37], whereby translational symmetry of a wave propagating through a periodic medium implies that the eigenvalue of the transfer matrix has the form $\lambda = e^{\pm ik_z a}$, where k_z is the propagation constant in the direction of periodicity and $a = d_L + d_H$ is the period of the multilayer (see Fig. 9). Note that an evanescent mode propagating within the reflector will have a complex k_z value, and $\lambda = e^{-k_z a}$ will be the rate of field decay. Note also that the Bloch theorem applies in the case of 1D translation symmetry such as for planar Bragg reflectors; however, it does not apply in the case of circular symmetry such as Bragg fibers. Nevertheless, in the asymptotic limit of Bessel functions the transfer matrix of a Bragg fiber simplifies into a form similar to that of planar multilayers and such an approximation has been shown to be valid even in the case of relatively small diameter Bragg fibers [42].

We therefore approximate the cladding of large diameter Bragg fibers by a simpler *planar* Bragg reflector and note that for smaller diameter Bragg fibers an analysis similar to the one presented here can be constructed using the asymptotic form of the Bragg fiber transfer matrix.

In a planar Bragg reflector the period is actually a bilayer of alternating high (n_H) and low (n_L) refractive index layers, and a transfer matrix containing plane wave elements can be constructed to describe the propagation through the bilayer. It can be shown [37,38] that a quadratic equation defines the eigenvalues (λ) of such a transfer matrix,

$$\lambda^2 - \lambda\Gamma_{\mathrm{TE,TM}} + 1 = 0, \tag{3}$$

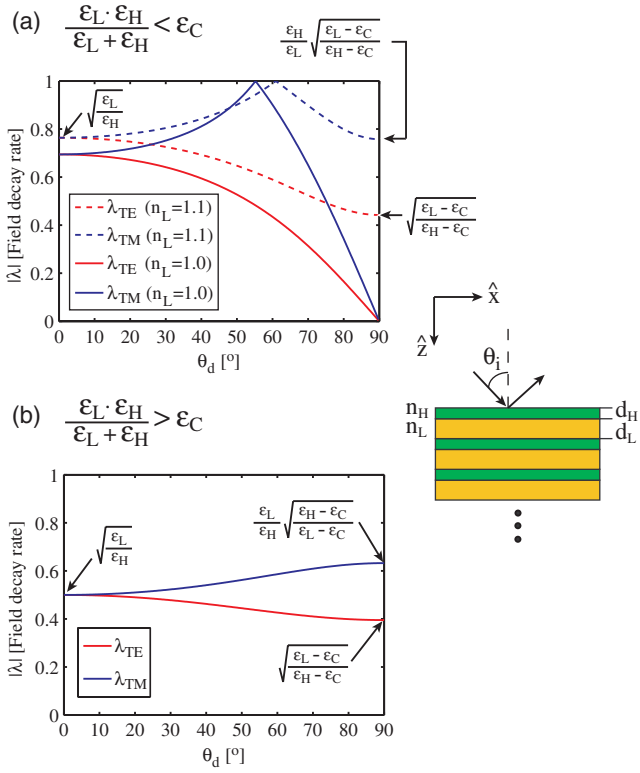

Fig. 9. (Color online) TE and TM field decay rates per bilayer for quarter-wave planar Bragg reflectors. The quarter-wave condition is assumed to be satisfied for each of the designed angles of incidence θ_d. Shown are the decay rates in two distinct regimes of operation. (a) $\frac{\epsilon_L \epsilon_H}{\epsilon_L + \epsilon_H} < \epsilon_c$, $n_C = 1.0$, $n_H = 1.5$. (b) $\frac{\epsilon_L \epsilon_H}{\epsilon_L + \epsilon_H} > \epsilon_c$, $n_C = 1.0$, $n_L = 1.5$, $n_H = 3.0$.

$$\Gamma_{\mathrm{TE,TM}} = 2\cos(\phi_L)\cos(\phi_H) - (r_{\mathrm{TE,TM}} + r_{\mathrm{TE,TM}}^{-1})\sin(\phi_L)\sin(\phi_H), \quad (4)$$

$$\phi_L = k_z^L d_L, \qquad \phi_H = k_z^H d_H, \quad (5)$$

$$r_{\mathrm{TE}} = \frac{k_z^L}{k_z^H}, \qquad r_{\mathrm{TM}} = \frac{\epsilon_H k_z^L}{\epsilon_L k_z^H}, \quad (6)$$

$$k_z^L = \sqrt{k_0^2\epsilon_H - k_x^2}, \qquad k_z^L = \sqrt{k_0^2\epsilon_H - k_x^2}, \quad (7)$$

$$\epsilon_L = n_L^2, \qquad \epsilon_H = n_H^2, \quad (8)$$

$$k_x = n_C k_0 \sin(\theta_i). \quad (9)$$

where d_L and d_H are, respectively, the thicknesses of the low- and high-index layers. θ_i is the incidence angle upon the reflector, c is the speed of light, $k_0 = \frac{2\pi f}{c}$, f is the frequency, and n_C is the refractive index of the ambient medium outside of the reflector (the core index in the case of a Bragg waveguide). From Eq. (3) and the Bloch theorem, we have

$$\lambda_1 = \frac{\Gamma_{\mathrm{TE,TM}}}{2} + \sqrt{\left(\frac{\Gamma_{\mathrm{TE,TM}}}{2}\right)^2 - 1}, \quad (10)$$

$$\lambda_2 = \frac{\Gamma_{\mathrm{TE,TM}}}{2} - \sqrt{\left(\frac{\Gamma_{\mathrm{TE,TM}}}{2}\right)^2 - 1}, \quad (11)$$

$$\lambda_1 = e^{ik_z a}, \qquad \lambda_2 = e^{-ik_z a}, \quad (12)$$

$$\lambda_1 + \lambda_2 = 2\cos(k_z a), \quad (13)$$

$$\cos(k_z a) = \frac{\Gamma_{\mathrm{TE,TM}}}{2}. \quad (14)$$

Equations (10), (11), and (14) completely characterize Bragg reflectors. When k_z is real, the eigenvalues (12) are complex exponentials, and the fields propagating within the reflector are Bloch waves and are said to be delocalized as there is transmission through the multilayer without change of amplitude. In other words, for such k_z values there is no reflection and the fields are radiated through the multilayer. These radiation bands can be found by plotting $|\cos(k_z a)| < 1$. When k_z is complex, instead of a delocalized state we have fields that are reflected and that decay exponentially within the multilayer at a rate λ^N, where N is the number of periods in the multilayer. These $|\cos(k_z a)| > 1$ regions define bandgaps where there is a reflection at a given frequency and incidence angle.

A. Ideal Bragg Reflectors

We begin by considering the design of idealized Bragg reflectors in order to elucidate the different operating regimes. It is well known that the most efficient reflector is a quarter-wave stack, wherein the constituent layers have an optical thickness of a quarter-wave, i.e. $\phi_L = \phi_H = \pi/2$. In such a case, Eqs. (10) and (11) reduce to the much simpler $|\lambda_1^{\mathrm{TE,TM}}| = r_{\mathrm{TE,TM}}$ and $|\lambda_2^{\mathrm{TE,TM}}| = r_{\mathrm{TE,TM}}^{-1}$. The solutions of interest require $|\lambda| < 1$. After some algebra we find,

$$\lambda_{\mathrm{TE}} = r_{\mathrm{TE}} < 1, \qquad \theta_i \in [0, \pi/2] \quad (15)$$

for the TE polarization. Moreover, for the TM polarization we find two regimes:

$$\frac{\epsilon_L\epsilon_H}{\epsilon_L + \epsilon_H} < \epsilon_c : \lambda_{\mathrm{TM}} = \begin{cases} r_{\mathrm{TM}}^{-1} & \theta \in [0, \theta_0] \\ r_{\mathrm{TM}} & \theta \in [\theta_0, \pi/2] \end{cases}, \quad (16)$$

$$\frac{\epsilon_L\epsilon_H}{\epsilon_L + \epsilon_H} > \epsilon_c : \lambda_{\mathrm{TM}} = r_{\mathrm{TM}}^{-1}, \qquad \theta \in [0, \pi/2] \quad (17)$$

$$\theta_0 = \arcsin\left(\sqrt{\frac{\epsilon_L\epsilon_H}{\epsilon_C(\epsilon_L + \epsilon_H)}}\right), \quad (18)$$

where θ_0 is the incidence angle which gives a Brewster angle *within* the multilayer stack.

To get a general sense of the Bragg fiber operating regimes, it is useful to examine the efficiency of an optimal planar quarter-wave stack by plotting the field decay rate $\lambda_{\mathrm{TE,TM}}$ as a function of an incidence angle θ_d at which the reflector is designed to operate. In other words, we examine the most efficient reflection that can be achieved at a given *design angle*. First, from the results in Fig. 9 it can be seen that λ_{TE} is always smaller than λ_{TM}, i.e. the field penetration within the multilayer is always higher for the TM polarization. Second, in the first regime ($\frac{\epsilon_L\epsilon_H}{\epsilon_L+\epsilon_H} < \epsilon_c$), we note the existence of a Brewster phenomenon. At the angle θ_0 the TM reflection within the multilayer becomes completely inefficient ($\lambda_{\mathrm{TM}} = 1$). Third, in the second regime ($\frac{\epsilon_L\epsilon_H}{\epsilon_L+\epsilon_H} > \epsilon_c$), the constituent refractive indices are such that the Brewster angle within the multilayer is avoided for all incidence angles and an omnidirectional reflection (at any incidence angle) can be achieved for both TE and TM polarizations simultaneously. Finally, an increase of the refractive index contrast ϵ_L/ϵ_H will reduce the value of $\lambda_{\mathrm{TE,TM}}$ in both regimes of operation whereas layer thicknesses different from the quarter-wave stack will increase it.

From the above considerations it is easy to understand that the TE_{01} mode of a Bragg fiber will always have lower loss than the TM_{01} mode. Since the hybrid modes are a mixture of TE and TM modes, the losses of the HE modes are dominated by the contribution of the lossier TM polarization. Thus, in order to guide a low-loss HE mode, the field decay of the TM polarization (λ_{TM}) must be reduced as much as possible. Whereas a planar Bragg reflector is generally designed to operate near normal incidence, a Bragg fiber is expected to operate at grazing angles of incidence. In Fig. 9 we see that there can be a substantial difference between the TM and TE field decay rates ($\lambda_{\mathrm{TM}}^N \gg \lambda_{\mathrm{TE}}^N$), where N is the number of bilayers in the Bragg reflector. Interestingly, Fig. 9(a) illustrates that the

$\frac{\epsilon_L\epsilon_H}{\epsilon_L+\epsilon_H} < \epsilon_c$ regime can significantly reduce λ_{TM} at grazing angles of incidence if $\epsilon_L \to \epsilon_C$.

In practice the thicknesses of a reflector are fixed and the quarter-wave condition cannot be satisfied for all wavelengths. So we now examine the actual behavior of planar Bragg reflectors as a function of operating frequency and incidence angle, for both operating regimes.

B. $\frac{\epsilon_L\epsilon_H}{\epsilon_L+\epsilon_H} > \epsilon_c$ Regime (Doped-Polymer Bragg Fiber)

A conventional method for examining a Bragg reflector is to plot its band diagram. In Fig. 10 the first row presents the band diagrams of doped-polymer Bragg reflectors, calculated using Eq. (14) and $|\cos(k_z a)| < 1$. The first column uses the parameters of the experimental TiO_2 doped-polymer Bragg fiber, whereas the second column presents a new design that will be explained in detail below. The red and blue bands are, respectively, the TE and TM admittance bands of the multilayer, whereas the white regions are the bandgaps where reflection occurs. Only the region above the black light lines should be considered, as it corresponds to the physically realizable incidence angles for real k_x [recall Eq. (9)], and the incidence angle increases as k_x goes from 0 to the light line. Since the Bragg fiber operates at grazing angles of incidence, the frequency bands of interest are the bandgaps along the light line. Note the excellent agreement between the planar reflector TE bandgaps along the light line of Fig. 10(a) and bandgap frequencies of the TE_{01} mode loss minima of the doped-polymer Bragg fiber shown in Fig. 7(a). Finally, the gray regions highlight frequency bands of omnidirectional reflection, where reflection can be achieved at any angle of incidence.

An interesting alternative method for examining Bragg reflectors is to plot the values of $\lambda_{TE,TM}$ within the bandgaps, in order to directly quantify the loss efficiencies of modes guided within those bandgaps. Such λ diagrams are presented in the second row of Fig. 10. Note that the white regions here correspond to bands of the reflector where $|\lambda| = 1$ because of the complex exponential λ values in those regions. It is easy to see that λ_{TE} decreases and λ_{TM} increases with increasing incidence angle (increasing k_x), and that λ_{TE} is smaller than λ_{TM}. This can also clearly be seen by taking a cut of the λ diagram along a fixed frequency, as shown in the third row of Fig. 10. Note that for $f = 0.88$ THz in Fig. 10(e) the values of $\lambda_{TE,TM}$ increase with decreasing incidence angle until reaching $\lambda = 1$ and cutting off when leaving the bandgap. This is due to the curvature of the bandgaps, where a mode at such a frequency will not be able to remain within the bandgap at all angles of incidence.

In Fig. 2 it is seen that doping with TiO_2 particles is a poor choice because the increase in refractive index is accompanied by a significant increase in the absorption loss. A more promising alternative is doping with metal particles. With small volume fractions below the percolation threshold (at a volume fraction ~1/3), the refractive index of the composite material can increase rapidly without an extraneous increase of absorption. Metal-dielectic composites have already been used at microwave frequencies to tailor material dielectric constants [43]. In the second column of Fig. 10 we propose a more efficient doping scheme using 25 vol.% Cu particles in polyethylene (PE), which yields an index $n > 3.0$ with losses $\alpha \le 1\,\mathrm{cm}^{-1}$. The smaller volume fraction of dopant particles should also facilitate the material processing and yield a composite with thermal and mechanical properties closer to that of pure PE.

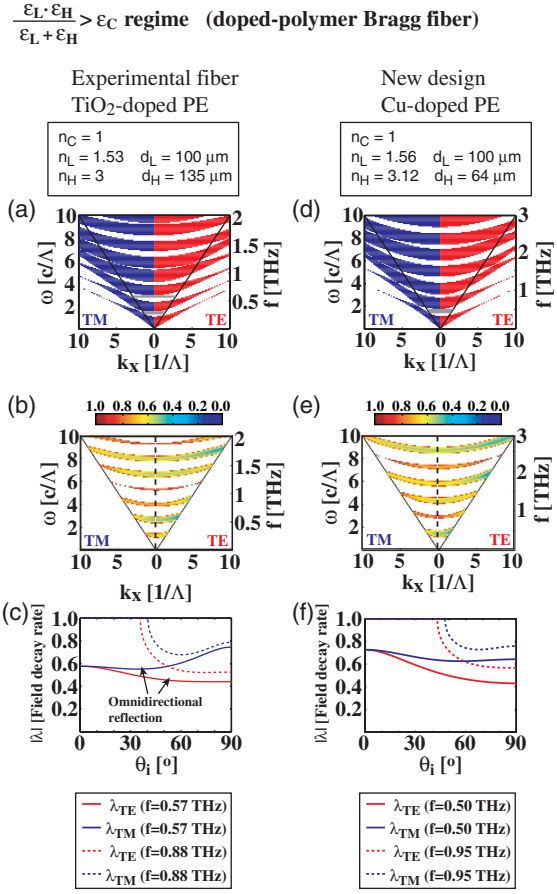

Fig. 10. (Color online) Band diagrams and field decay rates of doped-polymer planar Bragg reflectors ($\frac{\epsilon_L\epsilon_H}{\epsilon_L+\epsilon_H} > \epsilon_c$). First column uses parameters of experimental Bragg fiber, second column uses a quarter-wave design at $f = 0.49$ THz and $\theta_i = 0$. First row presents the band diagram of the reflectors. Second row presents λ-diagrams of the field decay rates within the bandgap regions. Third row presents cuts of the λ diagrams at constant frequencies.

C. $\frac{\epsilon_L\epsilon_H}{\epsilon_L+\epsilon_H} < \epsilon_c$ Regime (Air-Polymer Bragg Fiber)

Figure 11 presents the band diagrams and λ-diagrams of air-polymer planar Bragg reflectors operating in the $\frac{\epsilon_L\epsilon_H}{\epsilon_L+\epsilon_H} < \epsilon_c$ regime with $\epsilon_L = \epsilon_C$. The first column shows a calculation using the parameters of the experimental air-polymer Bragg fiber, illustrating a low-index contrast air-polymer fiber. The second column shows a calculation for a new design based on a high-index contrast air-polymer fiber. In the band diagrams, the closing of the TM bandgaps at the Brewster angle is seen to occur above the light line. Furthermore, in Fig. 11(a) the curvature of the bandgaps results in the absence of any omnidirectional reflections bands. Comparing Figs. 11(c) and 10(c), it can be seen that for grazing angles of incidence and for $f \sim 0.95$ THz that $\lambda_{TM} \sim 0.8$ for the doped-polymer reflector and $\lambda_{TM} \sim 0.6$ for the air-polymer Bragg fiber. Such a large difference in the field decay rate per bilayer leads to an order of magnitude difference in loss even with as few as $N = 5$ bilayers. This marked reduction of loss for the TM polarization helps explain why the HE mode losses are lower and more comparable to the TE mode losses in Fig. 6(a) than in Fig. 7(a).

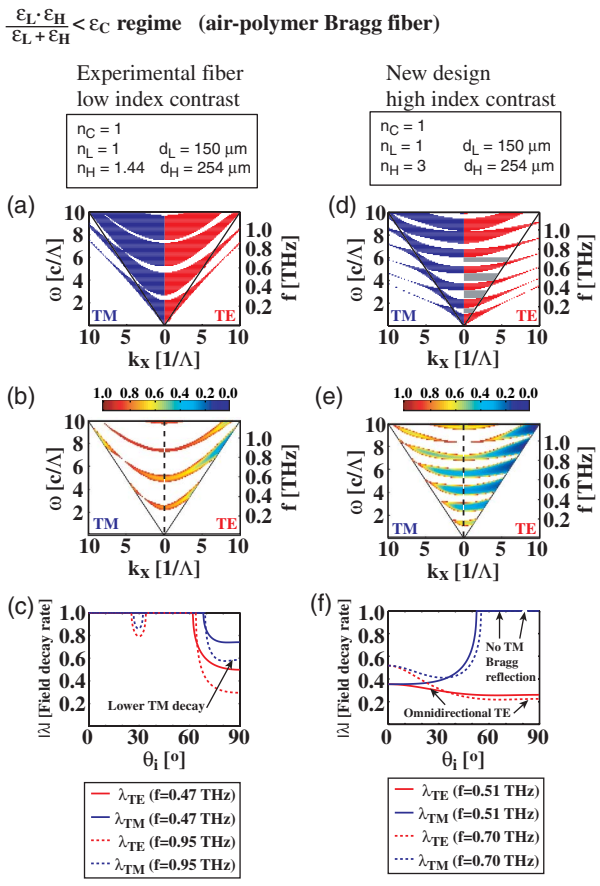

Fig. 11. (Color online) Band diagrams and field decay rates of air-polymer planar Bragg reflectors where $\epsilon_L = \epsilon_C\left(\frac{\epsilon_L\epsilon_H}{\epsilon_L+\epsilon_H} < \epsilon_c\right)$. First column uses parameters of experimental Bragg fiber, second column considers a 25 vol.% Cu-doped PE Bragg fiber. First row presents the band diagram of the reflectors. Second row presents λ diagrams of the field decay rates within the bandgap regions. Third row presents cuts of the λ diagrams at constant frequencies.

Finally, in the second row of Fig. 11 we present the interesting case where $\epsilon_L = \epsilon_C$ and the index contrast is high. In the band diagram it can be seen that the Brewster angle is increased and pushed close to the light line. In this case, the proximity of the Brewster angle to the light line increases the TM loss substantially at grazing angles of incidence. At low frequencies the TM polarization actually falls within the admittance bands of the multilayer and no TM Bragg reflections can occur. Therefore, the TM modes incur a greater propagation loss because of the Brewster angle phenomenon. On the other hand, the TE polarization exhibits very large bandgaps (larger than those of Fig. 10(d) and these are regions of omnidirectional TE reflection, as indicated by the gray regions. Furthermore, the values of λ_{TE} are extremely low and relatively flat as a function of incidence angle (indicating that the bending loss should be low). Such characteristics make this design an interesting candidate for a truly single-mode TE_{01} Bragg fiber. The mechanical stability of such a fiber could be increased by using a polymer foam instead of spacers for the low-index layers.

To further illustrate the potential of the newly proposed THz Bragg fiber designs, Fig. 12 plots the propagation loss and dispersion parameter for the first few modes. Narrow TM and HE bandgaps are seen to be guided despite the proximity of the Brewster angle to the light line. Further calculations (not shown) indicate that the TM bandgap disappears when the layer indices are changed such that the Brewster angle occurs exactly on the light line. A main point in Fig. 12 is that the propagation loss ($\alpha < 10^{-3}\,cm^{-1}$) and dispersion ($\beta_2 \ll 1\,ps/(THz \cdot cm)$) of the TE_{01} mode are significantly lower than those of the HE_{11} mode.

7. DISCUSSION

Recent developments in THz waveguides have lead to the demonstration of straight waveguide losses sufficiently low to start being useful ($\alpha \sim 0.01\,cm^{-1}$). However, to truly be practical a waveguide should have low bending losses and this factor will ultimately be the discriminant between different waveguiding strategies. An intuitive understanding of the bending losses of the waveguides presented in this paper can be gained be considering that, from a ray-optic perspective within large-core waveguides, bending will result in a decrease of the incidence angle of a ray. Consequently, the field decay rates plotted in Figs. 10(c) and 11(c) offer insights into the bending loss. In Fig. 10(c) it is clear from the omnidirectionality of the reflection that the doped-polymer Bragg fiber will guide *some* light no matter what the bending radius and the relative flatness of the curves in the 60° – 90° range indicates that the bending loss will be comparable to the straight fiber propagation loss. In the case of the air-polymer Bragg fiber (Fig. 11(c)) it was shown that a lower HE mode loss was achieved by lowering the TM polarization loss, but the trade-off is foregoing the omnidirectional reflection. Thus, although the field decay rates are relatively flat for incidence angles in the 75° – 90° range, the bending losses of air-polymer Bragg fibers are expected to rise sharply after a certain critical bending radius.

It is clear from the transmission results that coupling in multimode waveguides is a critical issue. It is worth stressing that even in the case where coupling is optimized at the input, such that only one mode is excited, any perturbations to the multimode waveguide (diameter fluctuations, bending, etc.) will couple light into the lossier higher-order modes [44]. Therefore, it is worth studying the optimization of the fiber

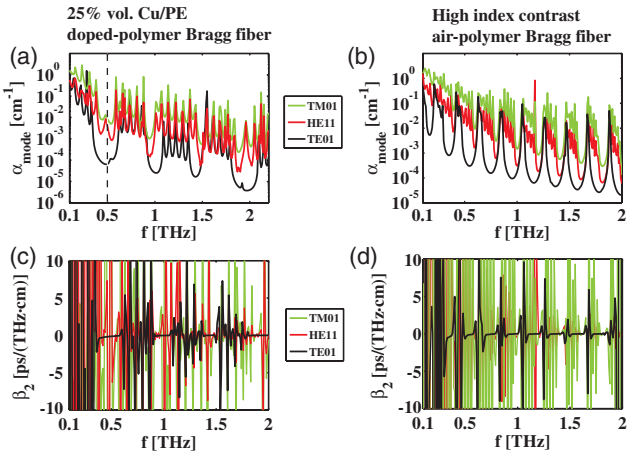

Fig. 12. (Color online) Propagation loss and dispersion parameter of the first few modes of the proposed Bragg fiber designs. First row, propagation losses α. Second row, β_2 dispersion parameter. First column, 25% Cu-doped PE doped-polymer Bragg fiber. Second column, high-index contrast air-polymer Bragg fiber.

design in the limit of a single-mode regime. Reducing the diameter of the core to achieve a single HE_{11} mode fiber is prohibited in the THz range by the large absorption loss. An interesting alternative is the *effectively* single-mode regime proposed by Bassett *et al.* [26], whereby all but the lowest-loss mode survives transmission over a certain range of fiber lengths. With a sufficiently small core to be close to the cutoff point of the TE_{02} mode, it should be possible to achieve a single TE_{01} mode operating regime requiring relatively short fiber lengths for the elimination of the other lossier modes. Nevertheless, Fig. 12 illustrates that even in an overmoded regime the transmission properties of the TE_{01} mode are superior to those of the HE_{11} mode. Researchers have shied away from considering the TE_{01} mode because of the azimuthally polarized source which is required for efficient excitation of that mode. However, the development of mode converters or new sources, such as a recently demonstrated photo-conductive antenna emitting a TE mode [45], could enable the development of such TE_{01} Bragg fibers.

8. CONCLUSION

In summary, we have fabricated and measured two very different types of hollow-core Bragg fibers. The first used air for the low-index layers whereas the second used a doped-polymer composite for the high-index layers. The doped-polymer Bragg fiber was shown to operate in a $\frac{\epsilon_L \epsilon_H}{\epsilon_L+\epsilon_H} > \epsilon_c$ regime where the high-index contrast leads to omnidirectional reflection. However, the HE_{11} losses were high and as a result the transmission was low with no clear bandgaps. On the other hand, the air-polymer Bragg fiber was shown to operate in a $\frac{\epsilon_L \epsilon_H}{\epsilon_L+\epsilon_H} < \epsilon_c$ regime. When $\epsilon_L = \epsilon_C$ the losses of the TM polarization decreased and enabled a low-loss HE_{11} mode to occur. Bandgap guidance could be seen in the transmission; however, coupling needs to be optimized to reduce multimode excitation. Both waveguides were shown to have straight waveguide propagation losses $\alpha < 0.05\,\mathrm{cm}^{-1}$ at certain peak transmission frequencies, but more work is required to resolve fabrication difficulties and to lower the loss over a broader range of frequencies. New fiber designs were proposed to address these issues, and the case was made for a TE_{01} THz Bragg fiber.

ACKNOWLEDGMENTS

This work was sponsored in part by a Natural Sciences and Engineering Research Council of Canada NSERC Alexander Graham Bell scholarship grant and by the Canada Institute for Photonics Innovations FP3 project. The authors would also like to acknowledge M. Robert Lemieux at the Industrial Materials Institute of the National Research Council of Canada for his assistance in extruding polyethylene film, as well as Jean-François Allard and Denis Morris at the University of Sherbrooke for their help with preliminary transmission measurements of THz Bragg fibers.

REFERENCES

1. M. Tonouchi, "Cutting-edge terahertz technology," Nat. Photon. **1**, 97–105 (2007).
2. W. L. Chan, J. Deibel, and D. M. Mittleman, "Imaging with terahertz radiation," Rep. Prog. Phys. **70**, 1325–1379 (2007).
3. K. Wang and M. Mittleman, "Metal wires for terahertz wave guiding," Nature **432**, 376–379 (2004).
4. L.-J. Chen, H.-W. Chen, T.-F. Kao, J.-Y. Lu, and C.-K. Sun, "Low-loss subwavelength plastic fiber for terahertz waveguiding," Opt. Lett. **31**, 308–310 (2006).
5. J. A. Harrington, "A review of IR transmitting, hollow waveguides," Fiber Int. Opt. **19**, 211–227 (2000).
6. S. G. Johnson, M. Ibanescu, M. Skorobogatiy, O. Weisberg, T. D. Engeness, M. Soljacic, S. A. Jacobs, J. D. Joannopoulos, and Y. Fink, "Low-loss asymptotically single-mode propagation in large-core OmniGuide fibers," Opt. Express **9**, 748–779 (2001).
7. R. Mendis and D. M. Mittleman, "Comparison of the lowest-order transverseelectric (TE_1) and transverse-magnetic (TEM) modes of the parallel-plate waveguide for terahertz pulse applications," Opt. Express **17**, 14839–14850 (2009).
8. J. A. Harrington, R. George, P. Pedersen, and E. Mueller, "Hollow polycarbonate waveguides with inner Cu coatings for delivery of terahertz radiation," Opt. Express **12**, 5263–5268 (2004).
9. T. Ito, Y. Matsuura, M. Miyagi, H. Minamide, and H. Ito, "Flexible terahertz fiber optics with low bend-induced losses," J. Opt. Soc. Am. B **24**, 1230–1235 (2007).
10. B. Bowden, J. A. Harrington, and O. Mitrofanov, "Fabrication of terahertz hollow-glass metallic waveguides with inner dielectric coatings," J. Appl. Phys. **104**, 093110 (2008).
11. R. Mendis and D. Grischkowsky, "THz interconnect with low-loss and low-group velocity dispersion," IEEE Microwave Wireless Comp. Lett. **11**, 444–446 (2001).
12. R. Mendis and D. M. Mittleman, "An ultra low loss THz waveguide," in *Conference on Lasers and Electro-Optics/Quantum Electronics and Laser Science Conference and Photonic Applications Systems Technologies*, OSA Technical Digest (CD) (Optical Society of America, 2008), paper CPDA5.
13. E. S. Lee, J. S. Jang, S. H. Kim, Y. B. Ji, and T.-I. Jeon, "Propagation of single-mode and multi-mode terahertz radiation through a parallel-plate waveguide," J. Korean Phys. Soc. **53**, 1891–1896 (2008).
14. H. Han, H. Park, M. Cho, and J. Kim, "Terahertz pulse propagation in a plastic photonic crystal fiber," Appl. Phys. Lett. **80**, 2634–2636 (2002).
15. M. Cho, J. Kim, H. Park, Y. Han, K. Moon, E. Jung, and H. Han, "Highly birefringent terahertz polarization maintaining plastic photonic crystal fibers," Opt. Express **16**, 7–12 (2008).
16. K. Nielsen, H. K. Rasmussen, A. J. Adam, P. C. Planken, O. Bang, and P. U. Jepsen, "Bendable, low-loss Topas fibers for the terahertz frequency range," Opt. Express **17**, 8592–8601 (2009).
17. Y. F. Geng, X. L. Tan, P. Wang, and J. Q. Yao, "Transmission loss and dispersion in plastic terahertz photonic band-gap fibers," Appl. Phys. B **91**, 333–336 (2008).
18. G. Ren, Y. Gong, P. Shum, X. Yu, J.-J. Hu, G. Wang, M. O. L. Chuen, and V. Paulose, "Low-loss air-core polarization maintaining terahertz fiber," Opt. Express **16**, 13593–13598 (2008).
19. C. S. Ponseca, R. Pobre, E. Estacio, N. Sarukura, A. Argyros, M. C. J. Large, and M. A. van Eijkelenborg, "Transmission of terahertz radiation using a microstructured polymer optical fiber," Opt. Lett. **33**, 902–904 (2008).
20. T. Hidaka, H. Minamide, H. Ito, J. Nishizawa, K. Tamura, and S. Ichikawa, "Ferroelectric PVDF cladding terahertz waveguide," J. Lightwave Technol. **23**, 2469–2473 (2005).
21. C.-H. Lai, Y.-C. Hsueh, H.-W. Chen, Y.-J. Huang, H.-C. Chang, and C.-K. Sun, "Low-index terahertz pipe waveguides," Opt. Lett. **34**, 3457–3459 (2009).
22. C.-S. Lai, B. You, J.-Y. Lu, T.-A. Liu, J.-L. Peng, C.-K. Sun, and H.-C. Chang, "Modal characteristics of antiresonant reflecting pipe waveguides for terahertz waveguiding," Opt. Express **18**, 309–322 (2010).
23. J.-Y. Lu, C.-P. Yu, H.-C. Chang, H.-W. Chen, Y.-T. Li, C.-L. Pan, and C.-K. Sun, "Terahertz air-core microstructure fiber," Appl. Phys. Lett. **92**, 064105 (2008).
24. M. Skorobogatiy and A. Dupuis, "Ferroelectric all-polymer hollow Bragg fibers for terahertz guidance," Appl. Phys. Lett. **90**, 113514 (2007).
25. R.-J. Yu, B. Zhang, Y.-Q. Zhang, C.-Q. Wu, Z.-G. Tian, and X.-Z. Bai, "Proposal for ultralow loss hollow-core plastic Bragg fiber with cobweb-structured cladding for terahertz waveguiding," IEEE Photon. Technol. Lett. **19**, 910–912 (2007).

26. I. Bassett and A. Argyros, "Elimination of polarization degeneracy in round waveguides," Opt. Express **10**, 1342–1346 (2002).
27. D. Turchinovich, A. Kammoun, P. Knobloch, T. Dobbertin, and M. Koch, "Flexible all-plastic mirrors for the THz range," Appl. Phys. A **74**, 291–293 (2002).
28. W. Withayachumnankul, B. M. Fischer, and D. Abbott, "Quarter-wavelength multilayer interference filter for terahertz waves," Opt. Commun. **281**, 2374–2379 (2008).
29. Y. Han, M. Cho, H. Park, K. Moon, E. Jung, and H. Han, "Terahertz time-domain spectroscopy of ultra-high reflectance photonic crystal mirrors," J. Korean Phys. Soc. **55**, 508–511 (2009).
30. S.-Z. A. Lo and T. E. Murphy, "Nanoporous silicon multilayers for terahertz filtering," Opt. Lett. **34**, 2921–2923 (2009).
31. C. Jansen, S. Wietzke, V. Astley, D. M. Mittleman, and M. Koch, "Fully flexible terahertz bragg reflectors based on titania loaded polymers," in *Conference on Lasers and Electro-Optics/Quantum Electronics and Laser Science Conference and Photonic Applications Systems Technologies*, OSA Technical Digest (CD) (Optical Society of America, 2008), paper CTuN1.
32. C. Jansen, F. Neubauer, J. Helbig, D. M. Mittleman, and M. Koch, "Flexible Bragg reflectors for the terahertz regime composed of polymeric compounds," in *Proceedings of IEEE Joint 32th International Conference on Infrared and Millimeter Waves and 15th International Conference on Terahertz Electronics*, (IEEE, 2007), pp. 984–986.
33. M. Ibanescu, Y. Fink, S. Fan, E. L. Thomas, and J. D. Joannopoulos, "An all-dielectric coaxial waveguide," Science **289**, 415–419 (2000).
34. Y. Fink, D. J. Ripin, S. Fan, C. Chen, J. D. Joannopoulos, and E. L. Thomas, "Guiding optical light in air using an all-dielectric structure," J. Lightwave Technol. **17**, 2039–2041 (1999).
35. Y.-S. Jin, G.-J. Kim, and S.-Y. Jeon, "Terahertz dielectric properties of polymers," J. Korean Phys. Soc. **49**, 513–517 (2006).
36. A. Dupuis, A. Mazhorova, F. Désévédavy, M. Rozé, and M. Skorobogatiy, "Spectral characterization of porous dielectric subwavelength THz bers fabricated using a microstructured molding technique," Opt. Express **18**, 13813–13828 (2010).
37. M. Skorobogatiy and J. Yang, *Fundamentals of Photonic Crystal Guiding*, (Cambridge University Press, 2009).
38. P. Yeh, A. Yariv, and C.-S. Hong, "Electromagnetic propagation in periodic stratified media. I. General theory," J. Opt. Soc. Am. **67**, 423–438 (1977).
39. S. Wietzke, C. Jansen, F. Rutz, D. M. Mittleman, and M. Koch, "Determination of additive content in polymeric compounds with terahertz time-domain spectroscopy," Polymer Testing **26**, 614–618 (2007).
40. S. Guo, S. Albin, and R. S. Rogowski, "Comparative analysis of Bragg fibers,",Opt. Express **12**,198–207 (2004).
41. K. Stoeffler, C. Dubois, A. Ajji, N. Guo, F. Boismenu, and M. Skorobogatiy, "Fabrication of all-plastic photonic bandgap Bragg fibers using rolling of PS/PMMA multilayer films," Polym. Eng. Sci. **50**, 1122–1127 (2010).
42. Y. Xu, R. K. Lee, and A. Yariv, "Asymptotic analysis of Bragg fibers," Opt. Lett. **25**, 1756–1758 (2000).
43. D. T. Zimmerman, J. D. Cardellino, K. T. Cravener, K. R. Feather, N. M. Miskovsky, and G. J. Weisel, "Microwave absorption in percolating metal-insulator composites," Appl. Phys. Lett. **93**, 214103 (2008).
44. M. Skorobogatiy, K. Saitoh, and M. Koshiba, "Full-vectorial coupled mode theory for the evaluation of macro-bending loss in multimode bers. Application to the hollow-core photonic bandgap fibers," Opt. Express **16**, 14945–14953 (2008).
45. S. Winnerl, B. Zimmermann, F. Peter, H. Schneider, and M. Helm, "Terahertz Bessel–Gauss beams of radial and azimuthal polarization from microstructured photoconductive antennas," Opt. Express **17**, 1571–1576 (2009).